



## Polymorphism in Non-Fullerene Acceptors Based on Indacenodithienothiophene

Item Type	Article
Authors	Marina, Sara;Scaccabarozzi, Alberto D.;Gutierrez-Fernandez, Edgar;Solano, Eduardo;Khirbat, Aditi;Ciammaruchi, Laura;Iturrospe, Amaia;Balzer, Alex;Yu, Liyang;Gabirondo, Elena;Monnier, Xavier;Sardon, Haritz;Anthopoulos, Thomas D.;Caironi, Mario;Campoy-Quiles, Mariano;Müller, Christian;Cangialosi, Daniele;Stingelin, Natalie;Martin, Jaime
Citation	Marina, S., Scaccabarozzi, A. D., Gutierrez-Fernandez, E., Solano, E., Khirbat, A., Ciammaruchi, L., ... Martin, J. (2021). Polymorphism in Non-Fullerene Acceptors Based on Indacenodithienothiophene. <i>Advanced Functional Materials</i> , 2103784. doi:10.1002/adfm.202103784
Eprint version	Post-print
DOI	<a href="https://doi.org/10.1002/adfm.202103784">10.1002/adfm.202103784</a>
Publisher	Wiley
Journal	Advanced Functional Materials
Rights	Archived with thanks to Advanced Functional Materials
Download date	2024-04-18 21:02:28
Link to Item	<a href="http://hdl.handle.net/10754/669509">http://hdl.handle.net/10754/669509</a>

## **Polymorphism in Non-Fullerene Acceptors Based on Indacenodithienothiophene**

*Sara Marina, Alberto D. Scaccabarozzi, Edgar Gutierrez-Fernandez, Eduardo Solano, Aditi Khirbat, Laura Ciammaruchi, Amaia Iturrospe, Alex Balzer, Liyang Yu, Elena Gabirondo, Xavier Monnier, Haritz Sardon, Thomas D. Anthopoulos, Mario Caironi, Mariano Campoy-Quiles, Christian Müller, Daniele Cangialosi, Natalie Stingelin and Jaime Martin\*.*

Sara Marina, Dr. Edgar Gutierrez-Fernandez, Elena Gabirondo Dr. Haritz Sardon and Dr. Jaime Martín.

POLYMAT, University of the Basque Country UPV/EHU Av. de Tolosa 72, 20018, San Sebastián, Spain

E-mail: [jaime.martin.perez@udc.es](mailto:jaime.martin.perez@udc.es)

Dr. Alberto D. Scaccabarozzi and Prof. Thomas Anthopoulos  
King Abdullah University of Science and Technology (KAUST)  
KAUST Solar Center (KSC)  
Thuwal 23955, Saudi Arabia

Dr. Alberto D. Scaccabarozzi and Dr. Mario Caironi  
Center for Nano Science and Technology@PoliMi, Istituto Italiano di Tecnologia, via Giovanni Pascoli 70/3, Milan 20133, Italy.

Dr. Eduardo Solano  
ALBA Synchrotron Light Source, NCD-SWEET Beamline, 08290 Cerdanyola del Vallès, Spain.

Aditi Khirbat, Alex Balzer and Prof. Natalie Stingelin  
School of Materials Science and Engineering and School of Chemical & Biomolecular Engineering, Georgia Institute of Technology, 311 Ferst Drive, Atlanta, Georgia, 30332, USA.

Dr. Amaia Iturrospe. Dr. Xavier Monnier and Dr. Daniele Cangialosi  
Centro de Física de Materiales (CFM) (CSIC-UPV/EHU), Materials Physics Center (MPC), Paseo Manuel de Lardizabal 5, San Sebastián, 20018, Spain.

Dr. Liyang Yu and Prof. Christian Müller  
Department of Chemistry and Chemical Engineering, Chalmers University of Technology, 41296  
Göteborg, Sweden.

Dr. Xavier Monnier and Dr. Daniele Cangialosi  
Donostia International Physics Center (DIPC), Paseo Manuel de Lardizabal 4, 20018 San Sebastián, Spain.

Dr. Laura Ciammaruchi and Dr. Mariano Campoy  
Instituto de Ciencia de Materiales de Barcelona (ICMAB-CSIC), Campus UAB, 08193 Bellaterra, Spain

Prof. Natalie Stingelin

Laboratoire de Chimie des Polymères Organiques–LCPO, UMR5629 Université de Bordeaux, Allée Geoffroy Saint Hilaire, Bâtiment B8 CS50023, 33615 Pessac Cedex, France.

Dr. Jaime Martin

Universidade da Coruña, Grupo de Polímeros, Departamento de Física e Ciencias da Terra, Centro de Investigacións Tecnolóxicas (CIT), Esteiro, 15471 Ferrol, Spain.

Ikerbasque, Basque Foundation for Science, 48013 Bilbao, Spain.

**Keywords:** Organic Electronics, NFAs, Polimorphism, Organic Semiconductors, Organic Solar Cells.

**Organic solar cells incorporating non-fullerene acceptors (NFAs) have reached remarkable power conversion efficiencies of over 18%. Unlike fullerene derivatives, NFAs tend to crystallize from solutions, resulting in bulk heterojunctions that include a crystalline acceptor phase. This must be considered in any morphology-function models. Here we confirm that high-performing solution-processed indacenodithienothiophene-based NFAs, i.e. ITIC and its derivatives ITIC-M, ITIC-2F and ITIC-Th, exhibit at least two crystalline forms. In addition to highly ordered polymorphs that form at high-temperatures, all the studied NFAs arrange into a low-temperature metastable phase that is readily promoted via solution processing and leads to the highest device efficiencies. Intriguingly, the low-temperature forms seem to feature a continuous network that favors charge transport despite of a poorly order along the  $\pi$ - $\pi$  stacking direction. Since the optical absorption of the structurally more disordered low-temperature phase can surpass that of the more ordered polymorphs while displaying comparable – or even higher – charge transport properties, we argue that such a packing structure is an important feature for reaching highest device efficiencies, thus, providing guidelines for future materials design and crystal engineering activities.**

## 1. Introduction

Organic solar cells (OSCs) have attracted great attention in the last 20 years as they promise cost effective, clean and renewable energy in addition to devices with complex form factors.<sup>[1]</sup> Most efficient OSCs include a blend of an electron donating semiconducting polymer and an electron accepting semiconducting small molecule arranged in a co-continuous phase-separated morphology known as bulk heterojunctions (BHJs).<sup>[2]</sup> Although fullerene derivatives have traditionally been the preferred choice for the realization of BHJs, so-called non-fullerene acceptors (NFAs) have recently emerged leading to significantly higher performances,<sup>[3]</sup> predominantly owing to a stronger absorption in the visible and near IR (NIR) regions and the surprisingly long excitons diffusion length.<sup>[4]</sup>

A highly successful example of a NFA is the indacenodithienothiophene-based molecule ITIC (chemical structure is shown in **Figure 1a**). Originally synthesized by Zhan et al. in 2015,<sup>[5]</sup> ITIC is an A-D-A structured molecule with indacenodithieno[3,2-b]thiophene (IT) as the central donor unit and with 2-(3-oxo-2,3-dihydroinden-1-ylidene)malononitrile (IC) as acceptor end groups. While ITIC delivered initially a relatively modest power conversion efficiency (PCE), optimization of device processing,<sup>[6]</sup> and incorporation of various chemical functionalities, such as fluorination (ITIC-2F, Figure 1b<sup>[7]</sup>), methylation (ITIC-M, Figure 1c<sup>[8]</sup>) or substitution of phenyl units by thiophene units (ITIC-Th, Figure 1d<sup>[9]</sup>), led to an increase of the PCE up to 14 %.<sup>[10]</sup>

Unlike fullerene derivatives,<sup>[11]</sup> NFAs, including ITIC-derivatives, often develop crystalline domains when they are solution-processed (e.g. by spin coating or wire-bar coating).<sup>[12]</sup> As a result, the solid-state microstructure and phase morphology of polymer:NFA BHJs often includes a crystalline acceptor phase, which must be considered in morphology/structure-function models of such OSCs, especially as NFAs often can crystallize in various polymorphs, i.e. in different crystal forms.<sup>[13]</sup> Accordingly, it is of utmost importance to identify the

structural, optical and electronic characteristics of the various crystalline phases NFAs can feature. However, few studies have addressed the often-rich phase behavior of these promising acceptor materials. Hence, the impact of the different crystalline forms on the electronic properties still remains unclearly understood.

Molecular polymorphism may affect device performance via different mechanisms: for example, different polymorphs can exhibit different optoelectronic properties because of different overlap between  $\pi$ -orbitals.<sup>[14]</sup> Moreover, crystal habits might differ between polymorphs, affecting the overall microstructure and leading to different BHJ phase morphologies.

The occurrence of polymorphism in organic materials, including organic semiconductors,<sup>[15]</sup> was originally rationalized in terms of the empirical Ostwald's rule of stages,<sup>[16]</sup> which states that in the crystallization of polymorphic systems, the most thermodynamically stable form is the last to appear. The polymorph initially formed is less thermodynamically stable but the activation energy required to overcome the barrier to form it is lower. In the case of solidification from solution, which is inherent to solution-processed organic semiconducting devices, this can be due to a favourable solvent-polymorph interfacial free energy.<sup>[15a]</sup>

Polymorphism might be closely connected to device efficiency in OSCs. Indeed, it has been recently reported that the slight increase in the degree of crystallinity of the ITIC domains in PBDB-T:ITIC BHJs, e.g., by thermal annealing below the glass transition temperature of ITIC ( $T_g^{\text{ITIC}} \sim 180 \text{ }^\circ\text{C}$ )<sup>[12c]</sup> by solvent annealing (with THF),<sup>[12b]</sup> or by the addition of solvent additives during the processing,<sup>[17]</sup> leads to the enhancement of both the device performance and device stability.<sup>[18]</sup> However, the increase in the degree of crystallinity achieved by annealing the devices at temperatures above the  $T_g$  of ITIC was detrimental, drastically reducing the PCE.<sup>[12c]</sup> To rationalize the above results, Yu et al.<sup>[12c]</sup> and Ciammaruchi et al.<sup>[19]</sup> have suggested that ITIC is able to crystallize into different polymorphs; i.e., a low temperature polymorph that

develops via diffusion limited crystallization at temperatures below  $T_g$  and a high-temperature polymorph that develops by regular cold crystallization at temperatures above the  $T_g$ .

In this paper, we identify, characterize and gain understanding of the crystalline forms of indacenodithienothiophene-based NFAs, namely ITIC, ITIC-M, ITIC-2F and ITIC-Th. We make the following key observations: we find that all four NFAs exhibit polymorphism, including a low-temperature metastable polymorph that is characterized by continuous 1D-chain or multidimensional mesh-like aromatic structures and seemingly poor structural order along the  $\pi$ - $\pi$  stacking direction. Since similar packing motifs have been reported for the best performing NFAs, including ITIC, IDTBR and the benchmark Y6,<sup>[13, 20]</sup> (molecular structure Figure S1 of the Supporting Information) our work suggests that these crystal forms are a common feature for the highest-performing electron acceptors for OSCs. We, thus, provide a rationale for future materials discovery. Indeed, our study reveals that these phases can exhibit higher optical absorption than the higher ordered, high-temperature polymorphs, and display comparable – or even higher – charge transport properties with respect to the latter.

## 2. Results and Discussion

We begin our discussion by identifying the different polymorphic phases in solution processed (spin cast) indacenodithienothiophene-based NFAs. Unless otherwise stated, the analyzed samples were 90 to 110-nm-thick films processed by spin coating 20 mg·mL<sup>-1</sup> solutions at 2000 rpm, which are standard processing conditions in OSC device manufacturing<sup>[7, 21]</sup> (see profilometry data in the Supporting Information Figure S2). We find that all spin cast indacenodithienothiophene-based NFAs exhibit polymorphism: three different polymorphs are found in case of ITIC, denoted as phase I, phase II and phase III, while ITIC-M, ITIC-2F and ITIC-Th exhibit two polymorphs, namely phase I and phase II. Low-temperature Phase I polymorphs develop in NFAs during casting under specific processing conditions (discussed in

detail later) while phase II polymorphs (and phase III in ITIC) are obtained upon thermal treatment. Grazing incidence wide angle X-ray scattering (GIWAXS) patterns of all crystal forms found in indacenodithienothiophene-based NFAs are shown in **Figure 1e-m** and Figures S4 and S5 of the Supporting Information. **Table I** summarizes the position and the crystal coherence length (CCL; calculated using the Scherrer equation<sup>[22]</sup> of the main diffraction peaks. In agreement with previous literature on NFAs packing motifs, the GIWAXS patterns for low-temperature Phase I forms of ITIC, ITIC-M, ITIC-2F and ITIC-Th are identified by multiple intense diffraction peaks in the low- $q$  region and few peaks in the high- $q$  region. In order to gain information about lattice characteristics and for peak indexing, the GIWAXS patterns were fitted with GIWAXS-SIIRkit<sup>[23]</sup> (details are included in the Supporting Information Figure S6 and Table S1). We note that our attempts to perform single crystal diffraction of Phase I crystals failed, which prevented us from conducting a more refined analysis of packing motifs.

The GIWAXS patterns found suggest packing motifs where NFA molecules pack into 1D-chain or multidimensional mesh-like structures, as those proposed previously for NFA single crystals [12d, 13a, 13b, 20, 24], which are expected to exhibit a high magnitude of electron transfer integral and therefore efficient charge transfer between molecules. Because 1D- or mesh-like packing motifs feature continuous aromatic structures that are separated by aliphatic domains,<sup>[13, 20]</sup> many large  $d$ -spacing symmetry planes exist, which are expected to give rise to multiple diffraction peaks in the low- $q$  region, as found in our patterns.<sup>[20d]</sup> This conjecture is further supported by our observation that the main aromatic-aliphatic periodicity peaks and the  $\pi$ - $\pi$  stacking – the signature of which are the intense diffraction peaks showing up at high- $q$  values – point both along the same direction (i.e., the out-of-plane direction), at least for low-temperature phases in ITIC, ITIC-M and ITIC-2F. Having aliphatic groups in ITIC-based NFAs pendant from the central building blocks, terminal acceptor groups are free to  $\pi$ - $\pi$  stack with

further terminal groups promoting continuous aromatic structures that result in 1D- or multidimensional structures.

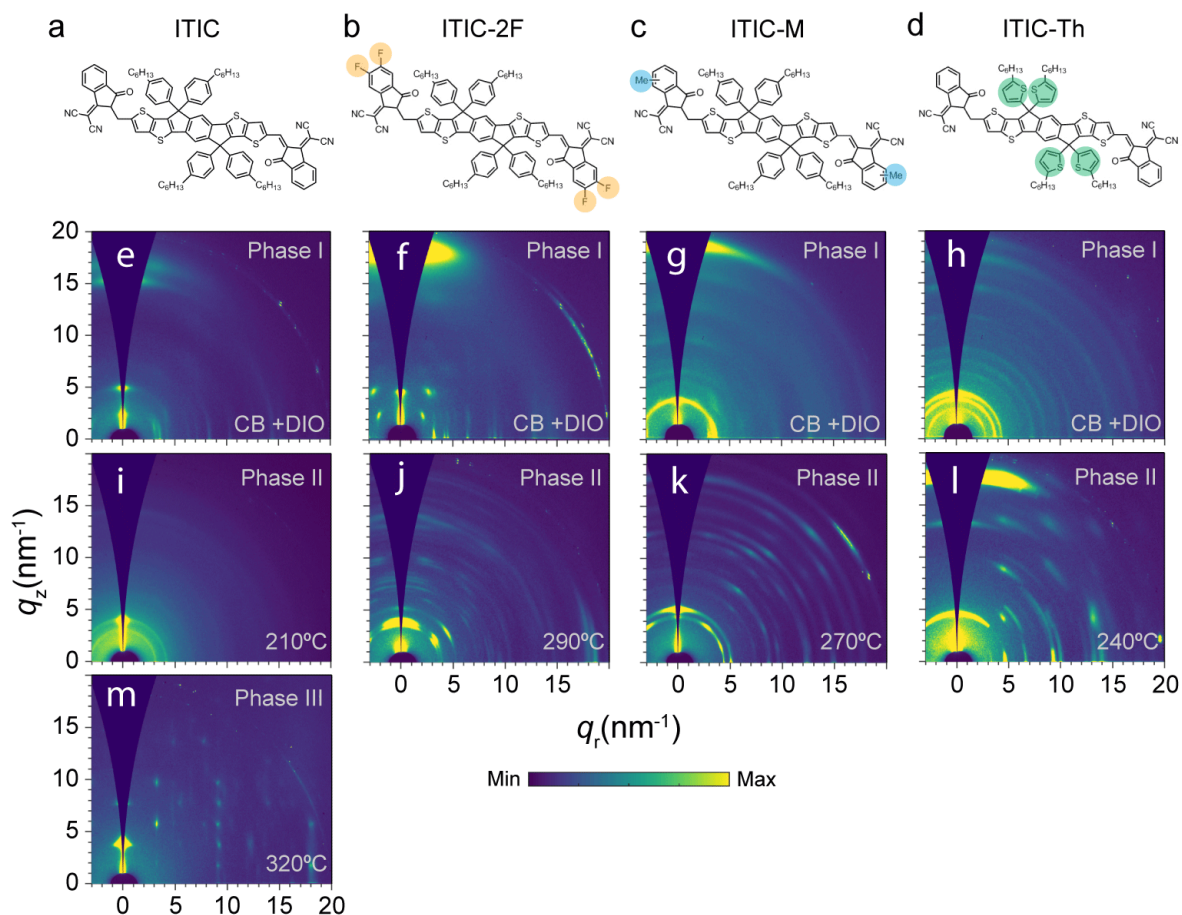


**Figure 1.** (a-d) Chemical structures of ITIC, ITIC-2F, ITIC-M and ITIC-Th, respectively. (e-m) 2D GIWAXS patterns for ITIC phase I (e), phase II (i) and phase III (m); ITIC-2F crystallized in phase I (f) and phase II (j); ITIC-M crystallized in phase I (g) and phase II (k); and ITIC-Th crystallized in phase I (h) and phase II (l). All phase I forms are produced by casting chlorobenzene (CB) solutions containing small amounts of DIO (0.5-1 %). Phases II and III are obtained by annealing the thin films at the temperatures indicated in each panel.

Low-temperature phase I polymorphs are promoted in films cast from aromatic solvents like chlorobenzene (CB), 1,2-orthodichlorobenzene (*o*-DCB) or 1,2-orthoxylyene (*o*-Xy). This can be deduced from the data obtained for both spin and drop-cast films (Figure S7, S8, S9 and S10 of the Supporting Information, respectively). We note that the ITIC-Th phase I can also be produced from dichloromethane (DCM) solutions. Nonetheless, ITIC-Th behaves slightly

different from the rest of NFAs. Moreover, we find that phase I is favored if a small amount of 1,8-diiodooctane (DIO), an additive frequently employed during processing of OSCs, is added to the casting solution (Figure S11 and S12 of the Supporting Information).<sup>[6-7, 10]</sup> This behaviour is most probably associated to the low vapor pressure of the DIO that allows more extensive NFA crystallization to occur prior to the vitrification of non-crystallized regions, i.e. DIO remains in the almost solidified film and acts as a plastiziser.<sup>[25]</sup>

**Table I.** Peak position and crystalline coherence length (CCL) values of the GIWAXS reflections for identified ITIC-X polymorphs when annealing *ex situ* the material at the relevant temperatures and cooling then to ambient temperature at 50 °C·min<sup>-1</sup>. \*CCL was calculated with Scherrer equation:  $CCL = 2 \cdot \pi \cdot k / \Delta q$  (k=0.9) and  $\Delta q$  as the full with half maximum of the given peak.

NFA	Polymorphs	periodic aromatic-aliphatic packing		$\pi$ - $\pi$ peak	
		$q(\text{nm}^{-1})$	CCL (nm)	$q(\text{nm}^{-1})$	CCL (nm)
ITIC	Phase I	3.2	23.2	15.5	4.0
		3.6	23.8		
		4.7	14.7		
		5.1	11.3		
	Phase II	3.2	24.0	/	/
		4.1	181		
Phase III	4.1	11.7	18.1	5.9	
ITIC-2F	Phase I	2.5	64.9	18.1	3.5
		3.2	29.7		
		4.2	24.4		
		4.6	16.1		
	Phase II	3.7	37.2	18.5	16.7
		4.1	23.4		
ITIC-M	Phase I	3.0	36.5	18.6	5.8
		3.8	15.5		
	Phase II	4.4	23.4		
		5.3	15.7		

		2.8	20.2		
ITIC-Th	Phase I	3.8	18.8	17.3	7.2
		4.4	18.2		
		4.7	16.1	17.9	7.4
	Phase II				

High temperature polymorphs, i.e. phase II (for ITIC-M and ITIC-2F) and phase III (for ITIC) exhibit, in general, a higher amount of well-defined diffraction peaks compared to phase I forms, which highlights that the former lattices exhibit more symmetry elements and, likely, larger ordered domains than their phase I counterparts. Phase II and III result when NFAs are thermally treated. For example, ITIC phase III develops at temperatures above 270 °C from phase I and at 220 °C from amorphous ITIC (Figure 1m and Figures S13 and S14 of the Supporting Information). ITIC phase II polymorph is obtained by heating phase I at intermediate temperatures between phase I and phase III (Figure 1i). Interestingly, the stability region for phase II seems to be dependent on the film thickness, which would agree with a thermotropic behaviour that is dependent on spatial confinement (Supporting Information Figure S13 and S14).<sup>[26]</sup> Lastly, phase II polymorphs develop during heating ITIC-M, ITIC-2F and ITIC-Th films at respectively, 220 °C, 220 °C and 170 °C (Figure S15 and S16 of the Supporting Information).

Dominant interactions between organic semiconducting molecules, including the ITIC derivatives studied here, are in general weak, e.g. van der Waals,  $\pi$ - $\pi$  interactions, hydrogen bonds and/or electrostatic interactions, which, in addition, are frequently non-specific. This results in the general tendency of organic semiconductors to adopt multiple packing modifications upon solidification.<sup>[15a]</sup> Moreover, the main chemical difference between these NFAs – at least ITIC, ITIC-M y ITIC-2F – results from their terminal acceptor groups that can lead to intermolecular interactions. Hence, the differences in the physicochemical characteristics of terminal groups (e.g. electronegativity, volume), resulting from the different

chemical functionality, might alter the intermolecular packing and, eventually, the development of a diverse polymorph set.

Interestingly, the phase behavior of ITIC-Th seems to differ from that of the other NFAs (as already alluded to above), possibly because the different chemical moiety in ITIC-Th is in the central building block and not in the terminal groups. More specifically, unlike the low-temperature phase I of ITIC, ITIC-M, ITIC-2F, the GIWAXS patterns for ITIC-Th phase I do not exhibit an intense and broad  $\pi$ - $\pi$  peak. This observation agrees with the packing motif reported for  $\beta$ -ITIC-Th single crystals<sup>[13a]</sup>. The high-temperature phase II, however, shows a clearer  $\pi$ - $\pi$  stacking signal, which is likely related to the  $\alpha$ -ITIC-Th lattice reported in Ref. <sup>[20b]</sup>. Moreover, our patterns for ITIC-Th phase I and phase II are similar to those reported in Ref. <sup>[12d]</sup>, where such a phase I pattern was interpreted as resulting from co-crystallization of ITIC and ITIC-Th into chain like packing structures. Even if the formation of chain-packing structures seems possible, our data suggests that the patterns correspond to two different ITIC-Th polymorphs.

In order to gain understanding of the polymorphism of indacenodithienothiophene-based NFAs from a thermodynamic viewpoint, temperature-resolved *in situ* GIWAXS and differential scanning calorimetry (DSC) experiments were conducted (heating rate was 10 and 20 °C·min<sup>-1</sup> respectively). Here, we will base our discussion on the data obtained for ITIC, which is shown in **Figure 2**, while the corresponding results for the remaining derivatives are included in Figure S15 of the Supporting Information (it should be stressed, however, that ITIC exhibits one more polymorph than the other derivatives). We must note here again that ITIC-Th seems to exhibit a different thermotropic behavior compared to the rest of NFAs. We argue, using an energy diagram depicted in Figure 2d, that phase I polymorphs (of ITIC, ITIC-M and ITIC-2F) are thermodynamically metastable whereas high temperature phase II and phase III are thermodynamically stable-phases. We base our hypothesis that phase I forms are metastable on

the following main arguments: (i) phase I melts before evolving into phase II. Clear indications of the above are the loss of birefringence (Figure 2a), the loss of Bragg diffractions at about 180 °C (Figure 2b) and the presence of an endothermic peak in DSC in the same temperature region (Figure 2c). (ii) Phase I is not formed during cooling. We deduce this from the POM data in Figure S17, S18 S19 and S20 of the Supporting Information and the GIWAXS data given in, e.g., Figure 1, which displays the patterns of phases II and III acquired from samples that were first thermally annealed (for 5 min) at the temperatures indicated and then cooled to 25 °C at 50 °C·min<sup>-1</sup>. As for ITIC-Th, or data shown in Figures S15 and S16 of the Supporting Information evidence that contrarily to the rest of Phase I forms, ITIC-Th Phase I melts at similar temperatures as Phase II (i.e. 240-260 °C). Thus, once Phase I is achieved from solution casting, ITIC-Th does not transform into phase II. Phase II just grows by cold crystallization from molten ITIC-Th at temperatures above T<sub>g</sub>.

Being thermodynamically metastable, the phase I crystal form of ITIC, ITIC-M and ITIC-2F, which is the predominant phase reported in many devices,<sup>[12c, 12d]</sup> is expected to evolve with time into the thermodynamically stable phase, i.e. phase II, which can compromise the long-term stability of the OSC devices. However, this seems not to occur during the lifetime of the devices. Indeed, a film stored for 2 years (in ambient conditions) still was solely comprised of the phase I crystals (results included in the Supporting Information Figure S21). Indeed, while we did not observe changes in film structure when storing samples at ambient conditions for over 2 years, we cannot exclude that during device operation and exposure to sun light (and, thus, heat), phase I may gradually transform in either phase II or III.

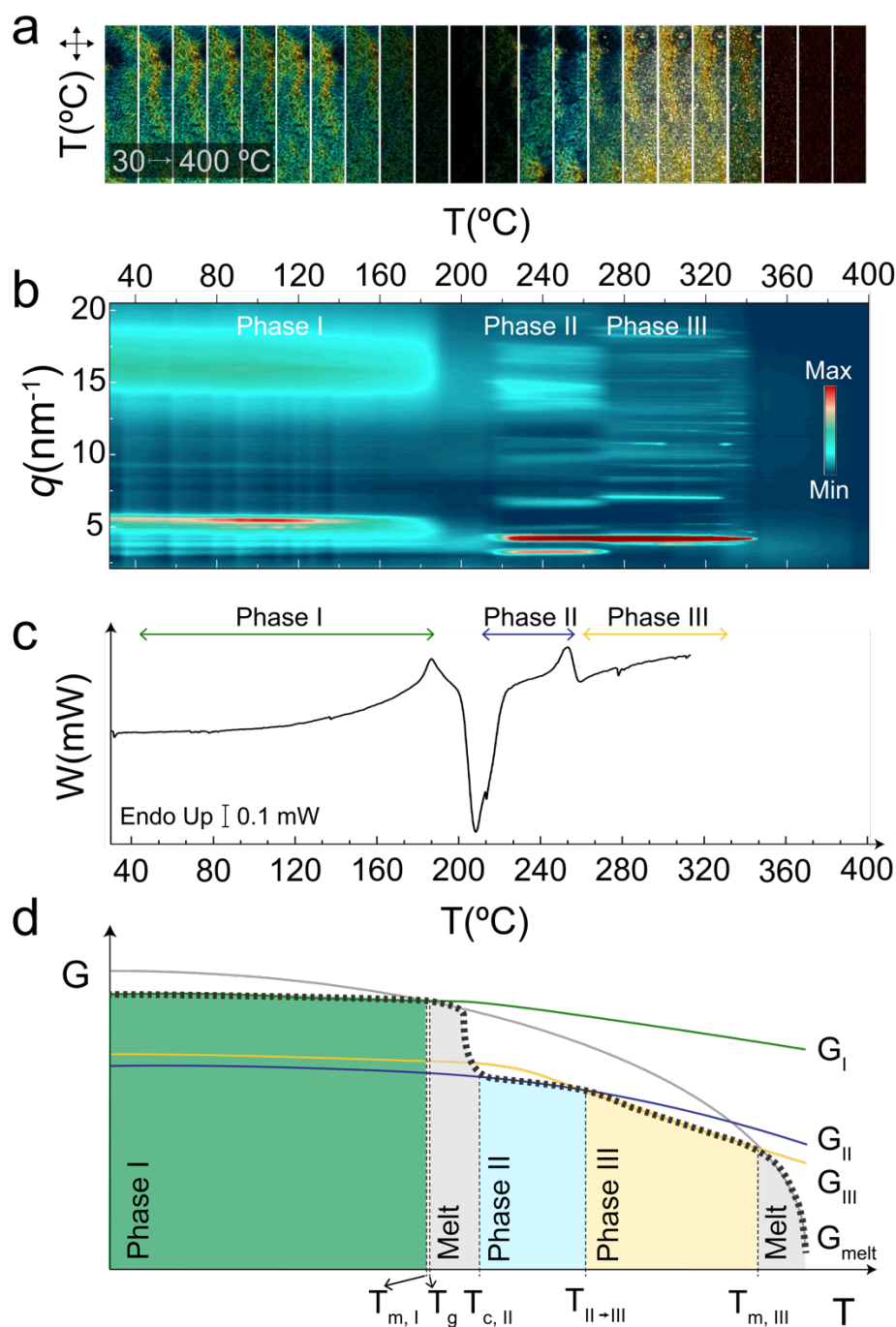


**Figure 2.** (a) Polarized optical microscopy (POM) images of a drop cast ITIC thin film acquired during a heating ramp from 30 °C to 400 °C at 10 °C·min<sup>-1</sup> under N<sub>2</sub> flow (the acquisition temperatures, T, are indicated in the micrographs). The size of the micrographs in the horizontal direction corresponds to 100 μm. (b) Contour plot of the of azimuthal integrations 2D GIWAXS patterns (from a 20 mg·mL<sup>-1</sup> chlorobenzene solution) acquired from room temperature up to 400 °C at 10 °C·min<sup>-1</sup> recorded for a drop cast ITIC film. (c) DSC 1<sup>st</sup> heating scan (from a 10 mg·mL<sup>-1</sup> chlorobenzene solution) acquired during a heating ramp from -50 °C to 320 °C at 20 °C·min<sup>-1</sup> (d) Schematic free energy (G) versus temperature (T) diagram for ITIC crystalline phases. The green, blue, yellow and grey solid lines correspond to the free energy for the phase I, the phase II, the phase II and the ITIC melt (G<sub>m</sub>), respectively. The dashed red line describes the evolution of G for a 100 % crystalline ITIC during heating. T<sub>m,I</sub>, T<sub>c,II</sub>, T<sub>II→III</sub>, and T<sub>m,III</sub>

represent the phase transition temperatures from phase I to molten ITIC, from phase II to phase III and from phase III to ITIC melt, respectively.

As tellingly, phase II is a thermodynamically stable form, because (i) it develops directly from the melt at about 210 °C and (ii) the polymorphic transition between phase II and phase III seems to be enantiotropic, which means that phase II and phase III are both thermodynamically stable in their respective temperature ranges. We argue the above based on the fact that the transition is recorded as an endothermic peak during heating (Figure 2c) and the transition is reversible, i.e. the reverse transition from phase III to phase II is detected during cooling (Supporting Information Figure S22 and S23). Phase III, however, would correspond to the thermodynamically preferred crystalline phase in ITIC because, it is the last form to evolve prior to the solid-melt transition, and it develops independently of the processing conditions applied (see Figures S4, S13 and S14 in the Supporting Information).

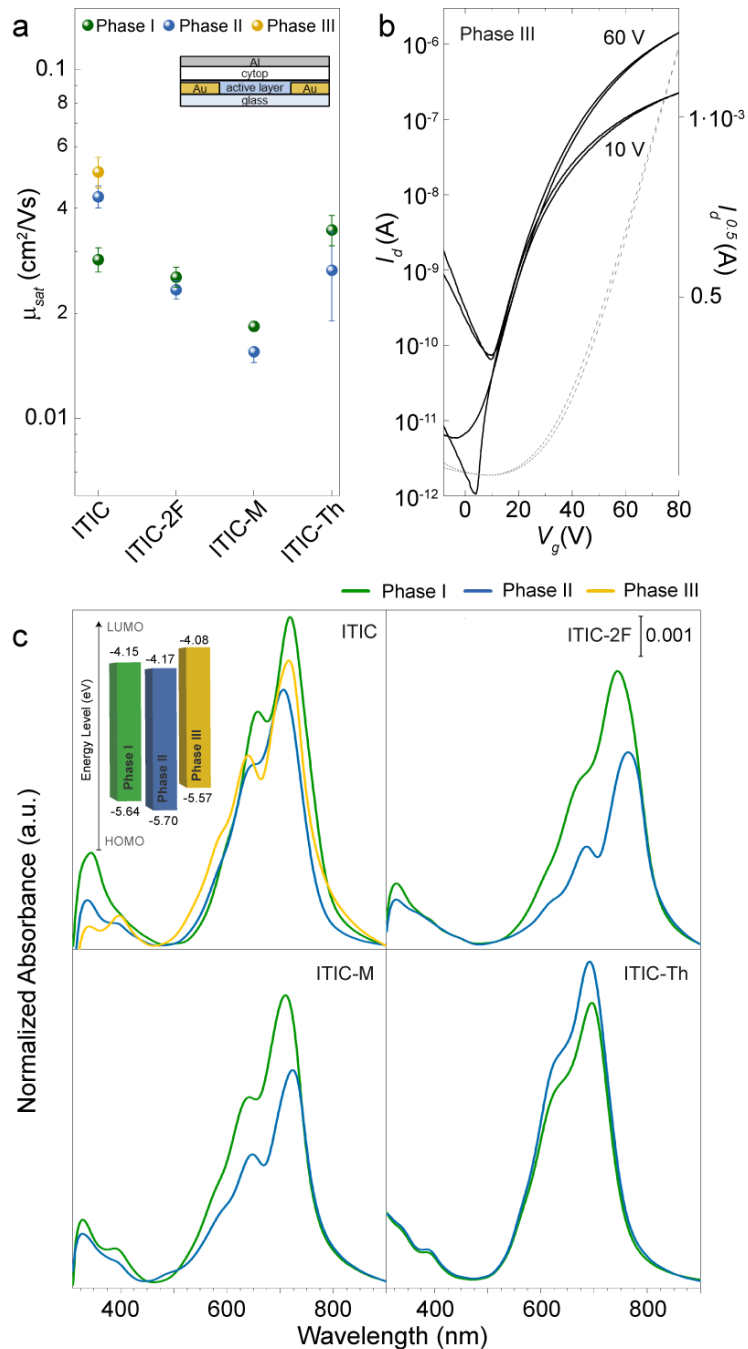


**Figure 3.** (a) Saturation field-effect mobility,  $\mu_{\text{sat}}$ , values measured for the different ITIC polymorphs. The inset shows a schematic of the OFET device architecture used. (b) Representative transfer characteristic of ITIC phase III (annealed at 270 °C for 5 min) in the linear ( $V_d = 10$  V) and saturation ( $V_d = 60$  V) regimes. Dashed line corresponds to the square root of the current in saturation regime is shown. (c) Room temperature UV-Vis absorption spectra for phase I (green lines), phase II (blue lines) and phase III (yellow lines) for ITIC, ITIC-2F, ITIC-M and ITIC-Th. The inset in the upper left panel shows the energetic levels for the three ITIC polymorphs found, as calculated from ultraviolet photoelectron spectroscopy (UPS) and UV-vis data.

Having rationalized the polymorphic behavior of ITIC-based NFAs, we went on to investigate the optoelectronic properties of the different polymorphs to gain insights why polymorph I phases generally lead to the highest-performing devices, as illustrated with devices comprising PBDB-T:ITIC and PBDB-T:ITIC-2F blends in the low-temperature phase I and high-temperature polymorphs (these data are included in the Supporting Information Figure S24). We first focused on the charge transport properties of the different polymorphs, hypothesizing that different molecular packing may affect the latter. For this purpose, we fabricated field-effect transistors (OFETs), using a top-gate bottom-contact device architecture, as shown in **Figure 3a**. Representative transfer characteristics curves for ITIC phase III, both in the linear ( $V_d=10V$ ) and saturation ( $V_d=60V$ ) regimes, from which the mobility values were extracted, are shown in Figure 3b, while the electrical characteristics of devices comprising the other polymorphs and molecules are included in the Supporting Information Figure S25, S26 and S27. All the devices display similar electrical characteristics, hence the different polymorphs in the four derivatives investigated exhibit comparable saturation field-effect mobilities ( $\mu_{sat}$ ), despite the seemingly inherent disorder along the  $\pi$ - $\pi$  stacking planes found in phase I polymorphs (Figure 3a and Figure S25 of the Supporting Information and Table II), which may be expected to limit charge transport. More precisely, Phase II and Phase III ITIC devices show a slight enhancement of the mobility compared to phase I devices, but the opposite trend is observed for ITIC-M, ITIC-2F and ITIC-Th, for which higher saturation mobility values are measured for phase I than for phase II. We argue that despite of the disorder of the  $\pi$ -stack, the continuous aromatic structures in phase I polymorphs facilitate long-range charge transport.

**Table II.** Relevant temperatures and optoelectronic parameters for the different microstructures identified in ITIC, ITIC-M, ITIC-2F and ITIC-Th. Optical band gap ( $E_g$ , estimated from  $E_g(eV) = h \cdot \nu \approx 1240/\lambda_{a.e.}(nm)$ ); Maximum absorption wavelength ( $\lambda_{max}$ ); Saturation field-effect mobility ( $\mu_{sat}$ ); Planks Constant ( $h$ ); Absorption edge values ( $\lambda_{a.e.}$ ); Frequency ( $\nu$ ).

	ITIC			ITIC-2F		ITIC-M		ITIC-Th	
	Ph I	Ph II	Ph III	Ph I	Ph II	Ph I	Ph II	Ph I	Ph II
$\mu_{\text{sat}}$ ( $\text{cm}^2/\text{Vs}$ )	0.028	0.043	0.05	0.025	0.023	0.018	0.016	0.034	0.027
$E_g$ (eV)	1.49	1.53	1.49	1.48	1.40	1.57	1.55	1.55	1.54
$\lambda_{\text{max}}$ (nm)	712	705	716	726	732	743	777	695	700

Intriguingly, strong differences in the optical absorption and emission of the NFA films crystallized in phase I, phase II and phase III were found in UV-Vis absorption and photoluminescence spectroscopy (PL) measurements (Figure 3c and Figure S28 of the Supporting Information, respectively). UV-vis absorption and PL measurements for each NFA were performed at room temperature on a single sample crystallized into phase I and phase II (and Phase III in the ITIC case), so that absorbed intensities for the different polymorphs are comparable (absorption and PL data are furthermore normalized to the thickness of each film). Our data clearly shows that the light absorption (and emission) is significantly stronger in phase I polymorphs than the high-temperature polymorphs, i.e. phase II in ITIC-2F, ITIC-M and ITIC-Th and phase II and III in ITIC. This is interpreted to result from an increased J-aggregate coupling in continuous aromatic structures found in Phase I forms. This could favour the performance of phase I compared to the other forms (phase II and III) in photovoltaic devices (device data is included in the Supporting Information Figure S24). However, we must also note that the higher performance of devices containing phase I may in addition originate from a more suitable donor:acceptor blend nanomorphology, i.e. a shorter phase separation length scale, as probed by GISAXS (Supporting Information Figure S29).

A further analysis of the absorption spectra reveals, moreover, that the absorption maxima ( $\lambda_{\text{max}}$ ) of the high-temperature polymorphs (phase II and III) appears, in general, to be slightly

red-shifted compared to that of phase I polymorphs. This results in lower optical band-gaps ( $E_g$ ) for the former phases (data are summarized in Table II). The phase II of ITIC is the exception (solid blue line in Figure 3c) as it exhibits a  $\lambda_{\max}$  and an absorption onset that is blue-shifted, resulting in a larger optical band-gap ( $E_g$ ).

The energetic levels of the ITIC polymorphs were assessed in more detail using ultraviolet photoelectron spectroscopy (UPS) (details are included in the Figure S31 of the Supporting Information). As shown in the inset of the upper panel in Figure 3c, the HOMO level of phase I is at 5.64 eV, that of phase II is at 5.70, and the one for phase III is at 5.57 eV. The LUMO levels, on the other hand, are at 4.15, 4.17, and 4.08 eV for phase I, phase II and phase III, respectively. Therefore, in principle, while differences exist, all polymorphs in ITIC exhibit relatively good energy level alignments relative to the donor polymers from the benzodithiophene-benzodithiophenedione-based donor copolymer family, such as PBDB-T<sup>[12b]</sup> (molecular structure in Figure S1 of the Supporting Information), thus, being an unlikely cause for phase I being better performing than phase II and III.

### 3. Conclusions

In summary, our work establishes that high-performing indacenodithienothiophene-based NFAs exhibit at least two crystalline phases: a low-temperature metastable polymorph that is characterized by continuous 1D-chain or multidimensional mesh-like, continuous aromatic structures and seemingly poor structural order along the  $\pi$ - $\pi$  stacking direction; and a highly ordered thermodynamically stable high-temperature phase (or phases, in the case of ITIC). Interestingly, packing motifs as found for the low-temperature polymorphs (continuous aromatic structures, poor  $\pi$ - $\pi$  stacking) seem to be a common feature among best performing OSCs, including ITIC, IDTBR and the benchmark Y6,<sup>[13,20]</sup> probably resulting from a chemical structure with aliphatic chains pendant from the central molecular building blocks while the

terminal acceptor groups are free to  $\pi$ - $\pi$  stack into a continuous network. The excellent device performance of phase I polymorphs is assigned to the fact that such structures exhibit a stronger light absorption than the high-temperature polymorphs (likely due to an increased J-aggregate coupling), while they display comparable – or even higher – charge transport properties with respect to the latter polymorphs, likely resulting from an increased electron transfer integral. Clearly, a fair comparison between the OPV performance between low temperature phase I and high-temperature phases is challenging to make because of the larger-scale phase separation that often accompanies the solid-solid phase transition from phase I to phase II and III polymorphs, which has a strong negative effect on device performance. Nonetheless, our results provide relevant and, likely, broadly applicable crystal engineering- and materials design guidelines. They also demonstrate that understanding of low temperature phase I polymorphs is critical in order to establish meaningful structure-function relationships for OSCs and to obtain insights, for instance, into the structural degradation mechanisms of NFA-based devices.

#### **4. Experimental Methods.**

*Materials:* The non-fullerene acceptor ITIC and the derivatives ITIC-M, ITIC-Th and ITIC- 2F were supplied by Ossila Ltd. Chlorobenzene (CB), *ortho*-dichlorobenzene (*o*-DCB), chloroform (CHCl<sub>3</sub>), dichloromethane (CH<sub>2</sub>Cl<sub>2</sub>), *ortho*-xylene (*o*-Xy) and 1,8-diiodooctane (DIO) were purchased from Merck and used as received.

*Sample preparation:* Solutions were spin-cast onto the substrate from a 20 mG·mL<sup>-1</sup> concentration in the specified solvent at a spin rate of 2000 rpm during 60s. For thick films, samples were directly drop-cast. The thermal treatments were performed as specified. The silicon substrates were positioned in a preheated hot stage (Linkam Scientific Instruments Ltd.) and annealed for 5 minutes. After heating, samples were cooled down at 50 °C·min<sup>-1</sup> to room temperature. The edges of the samples were removed to eliminate edge effects in the GIWAXS

experiment. (i) ITIC Phase I: CB + 1% DIO; phase II: CB + annealing at 210°C for 5 min, and phase III: CB + annealing at 320°C for 5 min. (ii) ITIC-2F Phase I: CB + 0.5% DIO; and phase II: CB + annealing at 290°C for 5 min (iii) ITIC-M Phase I: CB + 0.5% DIO; and phase II: CB + annealing at 270°C for 5 min. (iv) ITIC-Th Phase I: CB + 0.5% DIO; and phase II: CB + annealing at 240°C for 5 min.

*Grazing Incidence Wide Angle X-Ray Scattering (GIWAXS):* GIWAXS measurements were performed at the BL11 NCD-SWEET beamline at ALBA Synchrotron Radiation Facility (Spain). The incident X-ray beam energy was set to 12.4 eV using a channel cut Si (1 1 1) monochromator. The angle of incidence  $\alpha_i$  was set between 0.1-0.15 to ensure surface sensitivity. The scattering patterns were recorded using a Rayonix® LX255-HS area detector, which consists of a pixel array of 1920 × 5760 pixels (H × V) with a pixel size of 44 × 44  $\mu\text{m}^2$ . Data are expressed as a function of the scattering vector ( $q$ ), which was calibrated using Cr<sub>2</sub>O<sub>3</sub> as standard sample, obtaining a sample to detector distance of 145.6 mm. Temperature-resolved in situ X-ray experiments were performed using a Linkam® THMS 600 stage adapted for grazing incidence experiments. The heating rate used was 10 °C·min<sup>-1</sup> and the temperature difference between frames was 4 °C. Exposure times for in situ and ex situ experiments were 1 and 5 s, respectively. All the measurements were performed under N<sub>2</sub> atmosphere to minimize the damage of the films. 2D GIWAXS patterns were corrected as a function of the components of the scattering vector. Samples for GIWAXS were prepared by spin casting 20 mg·mL<sup>-1</sup> solutions on Si wafers at a spin rate of 2000 rpm. For thick film samples, the same solutions were directly drop casted. The thermal treatments were performed in a Linkam® hot stage under N<sub>2</sub> atmosphere. Edges of the samples were removed to eliminate edge effects in the GIWAXS experiment.

*Differential scanning calorimetry:* DSC was conducted under nitrogen at a scan rate of 20 °C·min<sup>-1</sup> with a Mettler Toledo STARe System DSC 3+ instrument.

*UV-Vis absorption spectroscopy:* UV-vis spectra were recorded with a Shimadzu UV-2550 spectrometer with a film adapter.

*Photoluminescence:* Photoluminescence spectra were recorded on a LS55 Perkin-Elmer Fluorescence spectrometer on the same samples analyzed by UV-vis.

*Ultraviolet Photoelectron Spectroscopy:* Ultraviolet Photoelectron Spectroscopy (UPS) was performed on a Kratos Axis Ultra XPS/UPS System using helium arc source with incident photon energy of 21.2 eV, a scan step size of 0.05 eV and a dwell time of 200 ms from 25 to -5 eV. The workfunction was calculated by linearly fitting the high binding energy cutoff to the intercept, which is subtracted from the incident energy, 21.2 eV. The energy from the Fermi edge to the HOMO level was calculated by linearly fitting the low binding energy cutoff to the intercept.

*Field-effect transistor fabrication and measurement:* A standard top-gate bottom-contact configuration was employed in the fabrication of field-effect transistors. Gold source/drain contacts were thermally evaporated on a borofloat glass after cleaning via ultrasonication in acetone and isopropanol and a subsequent O<sub>2</sub> plasma exposition at 100 W for 5 min. Solutions of the organic semiconductor were dissolved in chlorobenzene (10 mg·mL<sup>-1</sup>), stirred at 80 °C for two hours and then spin-coated in a nitrogen filled glovebox at 2000 rpm for 60 seconds. A Cytop® layer (~ 550 - 600 nm) was spin-coat on top of the semiconductor film at 4000 rpm, 400 rpm/sec for 90 seconds and then an annealing at 90 °C was performed for 1 hour. Al gate contact was finally thermally evaporated through a shadow mask. The devices were then tested in glovebox using a Keysight B2912A Precision Source/Measure Unit without exposing them to ambient conditions.

## **Acknowledgements**

This work is supported by the Ministerio de Ciencia e Innovacion/FEDER (under Ref. PGC2018-094620-A-I00 and PGC2018-095411-B-I00, CEX2019-000917-S and PGC2018-095411-B-100) and the Basque Country Government (Ref. PIBA19-0051). S.M. is grateful to POLYMAT for the doctoral scholarship. The authors thank A. Arbe, A. Alonso-Mateo, L. Hueso for their support and access to characterization tools. The authors also thank the technical and human support provided by SGIker of UPV/EHU and European funding (ERDF and ESF). GIWAXS experiments were performed at BL11 NCD-SWEET beamline at ALBA Synchrotron (Spain) with the collaboration of ALBA staff. J.M and E.F.-G. acknowledge support through the European Union's Horizon 2020 research and innovation program, H2020-FETOPEN 01-2018-2020 (FET-Open Challenging Current Thinking), 'LION-HEARTED', grant agreement n. 828984. J.M and N.S. would like to thank the financial support provided by the IONBIKE RISE project, which has received funding from the European Union's Horizon 2020 research and innovation programme under the Marie Skłodowska-Curie grant agreement No 823989. N.S. and A.K. and A.B. furthermore are grateful to the U.S. National Science Foundation (NSF) for support via project # 1905901 within NSF's Division of Materials Research. A. S. and M. C. acknowledge financial support by the European Research Council (ERC) under the European Union's Horizon 2020 research and innovation program "HEROIC," grant agreement 638059. This work was partially carried out at Polifab, the micro- and nanotechnology center of the Politecnico di Milano. .C.M. thanks the Knut and Alice Wallenberg Foundation for funding through the project "Mastering Morphology for Solution-borne Electronics".

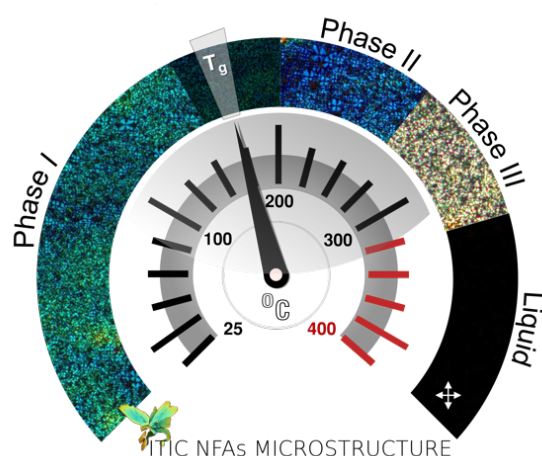
## References

- [1] N. S. Sariciftci, L. Smilowitz, A. J. Heeger, F. Wudl, *Science* **1992**, 258, 1474.

- [2] J. J. M. Halls, C. A. Walsh, N. C. Greenham, E. A. Marseglia, R. H. Friend, S. C. Moratti, A. B. Holmes, *Nature* **1995**, 376, 498.
- [3] Y. Firdaus, V. M. Le Corre, J. I. Khan, Z. Kan, F. Laquai, P. M. Beaujuge, T. D. Anthopoulos, *Advanced Science* **2019**, 6, 1802028.
- [4] a) C. Yan, S. Barlow, Z. Wang, H. Yan, A. K. Y. Jen, S. R. Marder, X. Zhan, *Nature Reviews Materials* **2018**, 3, 18003; b) Y. Lin, M. I. Nugraha, Y. Firdaus, A. D. Scaccabarozzi, F. Aniés, A.-H. Emwas, E. Yengel, X. Zheng, J. Liu, W. Wahyudi, E. Yarali, H. Faber, O. M. Bakr, L. Tsetseris, M. Heeney, T. D. Anthopoulos, *ACS Energy Letters* **2020**, 3663; c) Y. Lin, Y. Firdaus, F. H. Isikgor, M. I. Nugraha, E. Yengel, G. T. Harrison, R. Hallani, A. El-Labban, H. Faber, C. Ma, X. Zheng, A. Subbiah, C. T. Howells, O. M. Bakr, I. McCulloch, S. D. Wolf, L. Tsetseris, T. D. Anthopoulos, *ACS Energy Letters* **2020**, 5, 2935; d) Y. Firdaus, V. M. Le Corre, S. Karuthedath, W. Liu, A. Markina, W. Huang, S. Chattopadhyay, M. M. Nahid, M. I. Nugraha, Y. Lin, A. Seitkhan, A. Basu, W. Zhang, I. McCulloch, H. Ade, J. Labram, F. Laquai, D. Andrienko, L. J. A. Koster, T. D. Anthopoulos, *Nature Communications* **2020**, 11, 5220.
- [5] Y. Lin, J. Wang, Z.-G. Zhang, H. Bai, Y. Li, D. Zhu, X. Zhan, *Advanced Materials* **2015**, 27, 1170.
- [6] W. Zhao, D. Qian, S. Zhang, S. Li, O. Inganäs, F. Gao, J. Hou, *Advanced Materials* **2016**, 28, 4734.
- [7] W. Zhao, S. Li, H. Yao, S. Zhang, Y. Zhang, B. Yang, J. Hou, *Journal of the American Chemical Society* **2017**, 139, 7148.
- [8] S. Li, L. Ye, W. Zhao, S. Zhang, S. Mukherjee, H. Ade, J. Hou, *Advanced Materials* **2016**, 28, 9423.
- [9] Y. Lin, F. Zhao, Q. He, L. Huo, Y. Wu, T. C. Parker, W. Ma, Y. Sun, C. Wang, D. Zhu, A. J. Heeger, S. R. Marder, X. Zhan, *Journal of the American Chemical Society* **2016**, 138, 4955.
- [10] S. Zhang, Y. Qin, J. Zhu, J. Hou, *Advanced Materials* **2018**, 30, 1800868.
- [11] P. Westacott, N. D. Treat, J. Martin, J. H. Bannock, J. C. de Mello, M. Chabiny, A. B. Sieval, J. J. Michels, N. Stingelin, *Journal of Materials Chemistry A* **2017**, 5, 2689.
- [12] a) T. J. Aldrich, M. Matta, W. Zhu, S. M. Swick, C. L. Stern, G. C. Schatz, A. Facchetti, F. S. Melkonyan, T. J. Marks, *Journal of the American Chemical Society* **2019**, 141, 3274; b) Q. Liang, J. Han, C. Song, X. Yu, D.-M. Smilgies, K. Zhao, J. Liu, Y. Han, *Journal of Materials Chemistry A* **2018**, 6, 15610; c) L. Yu, D. Qian, S. Marina, F. A. A. Nugroho, A. Sharma, S. Hultmark, A. I. Hofmann, R. Kroon, J. Benduhn, D.-M. Smilgies, K. Vandewal, M. R. Andersson, C. Langhammer, J. Martín, F. Gao, C. Müller, *ACS Applied Materials & Interfaces* **2019**, 11, 21766; d) J. Mai, Y. Xiao, G. Zhou, J. Wang, J. Zhu, N. Zhao, X. Zhan, X. Lu, *Advanced Materials* **2018**, 30, 1802888.
- [13] a) S. Halaby, M. W. Martynowycz, Z. Zhu, S. Tretiak, A. Zhugayevych, T. Gonen, M. Seifrid, *Chemistry of Materials* **2021**, 33, 966; b) H. Lai, H. Chen, J. Zhou, J. Qu, M. Wang, W. Xie, Z. Xie, F. He, *The Journal of Physical Chemistry Letters* **2019**, 10, 4737; c) S. M. Swick, T. Gebraad, L. Jones, B. Fu, T. J. Aldrich, K. L. Kohlstedt, G. C. Schatz, A. Facchetti, T. J. Marks, *ChemPhysChem* **2019**, 20, 2608.
- [14] a) G. Giri, S. Park, M. Vosgueritchian, M. M. Shulaker, Z. Bao, *Advanced Materials* **2014**, 26, 487; b) G. Giri, E. Verploegen, S. C. B. Mannsfeld, S. Atahan-Evrenk, D. H. Kim, S. Y. Lee, H. A. Becerril, A. Aspuru-Guzik, M. F. Toney, Z. Bao, *Nature* **2011**, 480, 504; c) D. W. Davies, S. K. Park, P. Kafle, H. Chung, D. Yuan, J. W. Strzalka, S. C. B. Mannsfeld, S. G. Wang, Y.-S. Chen, D. L. Gray, X. Zhu, Y. Diao, *Chemistry of Materials* **2021**.
- [15] a) H. Chung, Y. Diao, *Journal of Materials Chemistry C* **2016**, 4, 3915; b) H. Chung, S. Chen, N. Sengar, D. W. Davies, G. Garbay, Y. H. Geerts, P. Clancy, Y. Diao, *Chemistry of Materials* **2019**, 31, 9115; c) H. Chung, S. Chen, B. Patel, G. Garbay, Y. H. Geerts, Y. Diao, *Crystal Growth & Design* **2020**, 20, 1646; d) Y. Diao, K. M. Lenn, W.-Y. Lee, M. A. Blood-Forsythe, J. Xu, Y. Mao, Y. Kim, J. A. Reinspach, S. Park, A. Aspuru-Guzik, G. Xue, P. Clancy, Z. Bao, S. C. B. Mannsfeld, *Journal of the American Chemical Society* **2014**, 136, 17046; e) G. E. Purdum, N. Yao, A. Woll, T. Gessner, R. T. Weitz, Y.-L. Loo, *Advanced Functional Materials* **2016**, 26, 2357; f) A. M. Hiszpanski, C. J. Dsilva, I. G. Kevrekidis, Y.-L. Loo, *Chemistry of Materials* **2018**, 30, 3330; g) G. E. Purdum, N. G. Telesz, K. Jarolimek, S. M. Ryno, T. Gessner, N. C. Davy, A. J. Petty, Y. Zhen, Y. Shu, A. Facchetti, G. E. Collis, W. Hu, C. Wu, J. E. Anthony, R. T. Weitz, C. Risko, Y.-L. Loo, *Journal of the American Chemical Society*

- 2018**, 140, 7519; h) G. Giri, R. Li, D.-M. Smilgies, E. Q. Li, Y. Diao, K. M. Lenn, M. Chiu, D. W. Lin, R. Allen, J. Reinspach, S. C. B. Mannsfeld, S. T. Thoroddsen, P. Clancy, Z. Bao, A. Amassian, *Nature Communications* **2014**, 5, 3573; i) J. Chen, M. Shao, K. Xiao, A. J. Rondinone, Y.-L. Loo, P. R. C. Kent, B. G. Sumpter, D. Li, J. K. Keum, P. J. Diemer, J. E. Anthony, O. D. Jurchescu, J. Huang, *Nanoscale* **2014**, 6, 449; j) L. Yu, N. Stingelin, *Journal of Organic Semiconductors* **2013**, 1, 16.
- [16] W. Ostwald, *Z. Phys. Chem.* **1897**, 22.
- [17] H. Chen, J. Qu, L. Liu, W. Chen, F. He, *The Journal of Physical Chemistry Letters* **2019**, 10, 936.
- [18] a) X. Du, T. Heumueller, W. Gruber, O. Almora, A. Classen, J. Qu, F. He, T. Unruh, N. Li, C. J. Brabec, *Advanced Materials*, n/a, 1908305; b) L. Ciammaruchi, O. Zapata-Arteaga, E. Gutiérrez-Fernández, J. Martín, M. Campoy-Quiles, *Submitted* **2020**.
- [19] L. Ciammaruchi, O. Zapata-Arteaga, E. Gutiérrez-Fernández, J. Martín, M. Campoy-Quiles, *Materials Advances* **2020**, 1, 2846.
- [20] a) L. Zhu, M. Zhang, G. Zhou, T. Hao, J. Xu, J. Wang, C. Qiu, N. Prine, J. Ali, W. Feng, X. Gu, Z. Ma, Z. Tang, H. Zhu, L. Ying, Y. Zhang, F. Liu, *Advanced Energy Materials* **2020**, 10, 1904234; b) H. Bristow, K. J. Thorley, A. J. P. White, A. Wadsworth, M. Babics, Z. Hamid, W. Zhang, A. F. Paterson, J. Kosco, J. Panidi, T. D. Anthopoulos, I. McCulloch, *Advanced Electronic Materials* **2019**, 5, 1900344; c) H. Lai, H. Chen, J. Zhou, J. Qu, P. Chao, T. Liu, X. Chang, N. Zheng, Z. Xie, F. He, *iScience* **2019**, 17, 302; d) D. Yan, W. Liu, J. Yao, C. Zhan, *Advanced Energy Materials* **2018**, 8, 1800204.
- [21] L. Gao, Z.-G. Zhang, H. Bin, L. Xue, Y. Yang, C. Wang, F. Liu, T. P. Russell, Y. Li, *Advanced Materials* **2016**, 28, 8288.
- [22] A. L. Patterson, *Phys. Rev.* **1939**, 56, 978.
- [23] V. A Savikhin, H.-G. A Steinruck, R.-Z. A Liang, B. A. A Collins, S. D. A Oosterhout, P. M. A Beaujuge, M. F. A Toney, *Journal of Applied Crystallography* **2020**, 53, 1108.
- [24] J. Qu, H. Chen, J. Zhou, H. Lai, T. Liu, P. Chao, D. Li, Z. Xie, F. He, Y. Ma, *ACS Applied Materials & Interfaces* **2018**, 10, 39992.
- [25] a) M. T. Fontana, H. Kang, P. Y. Yee, Z. Fan, S. A. Hawks, L. T. Schelhas, S. Subramaniyan, Y.-J. Hwang, S. A. Jenekhe, S. H. Tolbert, B. J. Schwartz, *The Journal of Physical Chemistry C* **2018**, 122, 16574; b) Y. Zhang, A. J. Parnell, F. Pontecchiani, J. F. K. Cooper, R. L. Thompson, R. A. L. Jones, S. M. King, D. G. Lidzey, G. Bernardo, *Scientific Reports* **2017**, 7, 44269.
- [26] J. Martín, M. Dyson, O. G. Reid, R. Li, A. Nogales, D.-M. Smilgies, C. Silva, G. Rumbles, A. Amassian, N. Stingelin, *Advanced Electronic Materials*, 1700308.

## TOC graphic:



**Non-fullerene acceptors used in organic solar cells often crystallize when they are cast from solution. Specifically, ITIC and its derivatives ITIC-M, ITIC-2F and ITIC-Th, exhibit a metastable form that is readily promoted via solution processing and leads to the highest device efficiencies despite exhibiting poor order along the  $\pi$ - $\pi$  stacking direction. These forms show high optical absorption and similar charge carrier mobility compared to the more ordered polymorphs.**